



Plasmon Ag/Na-doped defective graphite carbon nitride/NiFe layered double hydroxides Z-scheme heterojunctions toward optimized photothermal-photocatalytic-Fenton performance

Weifeng Kong^a, Zipeng Xing^{a,*}, Bin Fang^a, Yongqian Cui^a, Zhenzi Li^{b,*}, Wei Zhou^{a,b,**}

^a Department of Environmental Science, School of Chemistry and Materials Science, Key Laboratory of Functional Inorganic Material Chemistry, Ministry of Education of the People's Republic of China, Heilongjiang University, Harbin 150080, PR China

^b Shandong Provincial Key Laboratory of Molecular Engineering, School of Chemistry and Chemical Engineering, Qilu University of Technology (Shandong Academy of Sciences), Jinan 250353, PR China

ARTICLE INFO

Keywords:

Photocatalysis
G-C₃N₄
Z-scheme heterojunction
Layered double hydroxide
Photothermal effect

ABSTRACT

Three-dimensional flower-shaped plasmon Ag/Na-doped defective graphitic carbon nitride/NiFe layered double hydroxides (Ag/NaCNN/NiFe-LDH) Z-scheme heterojunction are fabricated by hydrothermal and calcination methods. The flower-shaped structure of NiFe-LDH enhances the multiple reflection and scattering of light, providing enough active sites to improve the utilization of sunlight. The introduction of Na-doped defects narrows the band gap of graphitic carbon nitride and accelerated the charge separation. Due to the surface plasmon resonance effect of Ag, Ag/NaCNN/NiFe-LDH shows excellent photothermal effect. The synergistic effect of photothermal-photocatalytic-Fenton reaction and Z-scheme heterojunction increased the hydrogen production of Ag/NaCNN/NiFe-LDH by 0.543 mmol h⁻¹, which was 10 times higher than that of NiFe-LDH. The degradation efficiency of p-nitrophenol and bisphenol A under visible light was 99%. This simple strategy and reasonable design provide new ideas for the construction of Z-scheme heterojunction photocatalysts.

1. Introduction

Energy shortage and environmental governance have always been hot issues of global concern [1,2]. As an advanced technology that can be directly used, clean and renewable solar energy can achieve high-efficiency degradation of pollutants, photocatalysis provides a new solution to energy and environmental problems [3,4]. Photocatalytic technology with the advantages of low-cost and simplicity could avoid secondary pollution. The common photocatalyst (TiO₂, Fe₂O₃, CdS, etc. [5–7]) not only exhibits good degradation ability in the removal of pollutants such as organic matters and heavy metals, but also has potential values in water splitting, carbon dioxide reduction, and nitrogen fixation. The layered double hydroxides (LDHs) have attracted much attention in photocatalysis due to their special layered structures [8]. LDHs also have structural controllability and interlayer anion exchange, which increases the flexibility of the electronic structure of LDHs and enhances the reaction rate [9–11]. Zhang et al. prepared CuZnAl-LDH

nanosheets via alkali-etched, which exhibited excellent photochemical properties in nitrogen fixation (0.41 mmol h⁻¹ NH₃ precipitation rate) under UV–VIS irradiation [12]. The two-dimensional sheet structure of NiFe-LDH was self-assembled to form a flower-shaped structure by hydrothermal method. The three-dimensional flower-shaped structure exposed a large number of surface-active sites, the large gaps formed between the sheet-like structures enhanced light reflection and scattering, and improved the utilization of solar energy [12]. Moreover, NiFe-LDH provides surface active sites as a linking bridge between NaCNN and Ag, which makes Ag/NaCNN/NiFe-LDH have good degradation ability and hydrogen production capacity.

Advanced oxidation process (AOPs), as a rapid removal technology of organic pollutants, has a good application prospect in the removal of refractory organic pollutants such as polycyclic aromatic hydrocarbons [13,14]. Among them, Fenton reaction is one of the important reactions in AOPs. According to the report photocatalysis combined with Fenton reaction is one of the best ways to solve the pollution problem of the ring

* Corresponding authors.

** Corresponding author at: Department of Environmental Science, School of Chemistry and Materials Science, Key Laboratory of Functional Inorganic Material Chemistry, Ministry of Education of the People's Republic of China, Heilongjiang University, Harbin 150080, PR China.

E-mail addresses: xingzipeng@hlju.edu.cn (Z. Xing), zhenzhenlee2014@163.com (Z. Li), zwchem@hotmail.com (W. Zhou).

<https://doi.org/10.1016/j.apcatb.2021.120969>

Received 26 August 2021; Received in revised form 19 November 2021; Accepted 25 November 2021

Available online 27 November 2021

0926-3373/© 2021 Elsevier B.V. All rights reserved.

river [15]. The constructed photocatalytic Fenton coupling system can enhance the absorption range of light, promote the separation photo-generated carriers, and improve the degradation ability of pollutants [16–18]. With the purpose of improving the photocatalytic performance of the NiFe-LDH, it could be combined with the advanced oxidation Fenton reaction. The Fenton reaction uses the chain reaction between Fe^{3+} and H_2O_2 to catalyze the formation of $\bullet\text{OH}$, and $\bullet\text{OH}$ has strong oxidizing properties, which can oxidize toxic and difficult-to-degrade organic compounds to small molecules. The photocatalytic-Fenton coupling system could improve charge separation and prolong carrier lifetime. When Fe^{3+} of NiFe-LDH is mixed with H_2O_2 , the oxidation ability and degradation rate of p-nitrophenol are enhanced obviously. In synergy, it can enhance the capture ability of photogenerated electrons, increase the oxidation rate of pollutants and thus improve the degradation ability of photocatalysts.

The photocatalytic performance of the single hydrotalcite material can not achieve the expected results, so graphitic carbon nitride ($\text{g-C}_3\text{N}_4$) is usually chosen for combining with hydrotalcite to improve the performance of the catalyst. $\text{g-C}_3\text{N}_4$ has visible light-inducing activity, good stability, easy synthesis, and low-cost, making it a promising material for photocatalysis, but its narrow light absorption range leads to low charge separation and conversion efficiency, which becomes a bottleneck in practical applications [19]. Heterostructure fabrication [20], elemental doping and defect modification [21,22], are conventional ways to improve the photocatalytic properties of $\text{g-C}_3\text{N}_4$. The doping of $\text{g-C}_3\text{N}_4$ with metal elements can change the electronic structure and band gap, which facilitates the transfer of charge carriers and improves the photocatalytic activity [23]. Doping of non-metallic elements such as S could improve the selectivity of $\text{g-C}_3\text{N}_4$ to produce H_2O_2 [24]. Defects in holes have been reported to inhibit charge recombination through electron trapping active sites [25,26]. $\text{g-C}_3\text{N}_4$ containing both Na doping defects (NaCNN) with narrowed band gap of 2.64 eV was reported, in which alkali doping and N vacancy narrowed the band gap and increased the charge transfer rate. Although the photocatalytic performance was improved obviously, the charge separation efficiency was still unsatisfactory.

Noble metal doping is also good approach to improve the performance of photocatalysts [27]. Surface plasmon resonance (SPR) can improve the light-to-heat conversion rate. The precious metal Ag has low-cost and high stability [28,29]. Therefore, the introduction of Ag to photocatalyst can greatly enhance the photocatalytic activity, because the ‘hot electrons’ excited by the SPR effect can be transferred from the surface of metal quantum dots to NiFe-LDH, thus promoting the separation of electrons and holes [30,31]. Kuila et al. synthesized the ternary composite $\text{Ag@AgVO}_3/\text{BiOCl}$ by hydrothermal method. Ag quantum dots promoted charge transfer and absorption in the visible light region, and the removal rate of methyl orange (MO) and Bisphenol A (BPA) was almost up to 100% [32]. Therefore, to fabricate multicomponent system with suitable band alignment for efficient charge separation and enhanced solar light absorption is still a challenge.

Here, we report a plasmon Ag/Na-doped defective graphitic carbon nitride/NiFe layered double hydroxides with three-dimensional flower-shaped by hydrothermal and calcination method. Through the band gap alignment and reasonable design, a Z-scheme heterojunction is constructed. The formation of Z-scheme heterojunction can effectively promote the migration and separation of photogenerated carriers. $\text{g-C}_3\text{N}_4$ with Na-doped defects extends the light absorption range and promotes charge separation by adjusting the band gap, thereby improving the photocatalytic performance. The SPR effect of plasmon Ag makes the photocatalyst have good photothermal performance. A photocatalytic-Fenton coupling system is also proposed, which has excellent performance in degrading pollutants. Through detailed characterization, the unique structure of Ag/NaCNN/NiFe-LDH ternary composite is proved, and the photocatalytic performance of Ag/NaCNN/NiFe-LDH and the performance of photocatalytic-Fenton degradation on high-toxic p-nitrophenol are evaluated.

2. Experimental section

Fig. 1a shows the synthesis process of Ag/NaCNN/NiFe-LDH. First, the flower-shaped NiFe-LDH and the sheet-shaped NaCNN were prepared, then the prepared mixed solution of NiFe-LDH and NaCNN were added to the reactor to obtain NaCNN/NiFe-LDH. Finally, the final product Ag/NaCNN/NiFe-LDH was obtained under the irradiation of Xenon lamp after introducing Ag.

2.1. Synthesis of NaCNN

Firstly, the $\text{g-C}_3\text{N}_4$ nanosheets were prepared by the thermal polycondensation method. In a typical synthesis, melamine (10 g) was placed in a muffle furnace at 550 °C and calcined at a heating rate of 3 °C min^{-1} for 4 h, and cooled naturally to obtain a light-yellow powder. The light-yellow powder was further calcined at 600 °C at a rate of 2 °C min^{-1} for 1 h to obtain $\text{g-C}_3\text{N}_4$ nanosheets. Then 0.6 g of $\text{g-C}_3\text{N}_4$ and 4.28 g of NaCl were ground together in a mortar, and the mixture was calcined in a tube furnace, increasing at a rate of 5 °C min^{-1} , and heated at 450 °C for 2 h. The resulting powder was then heated in water at 100 °C for 4 h to remove the metal salt, subsequently collected by centrifugation, and dried in an oven. The dried powder was washed in a 1 mol/L hydrochloric acid aqueous solution for 1 h to obtain a defective graphitic carbon nitride (CNN) containing N-deficient. Finally, CNN was mixed with 1 mol/L NaOH solution for 1 h, collected by centrifugation and dried. The powder obtained was carbon nitride with alkali metal Na-doping.

2.2. Synthesis of NiFe-LDH

After adding $\text{Ni}(\text{NO}_3)_2 \cdot 6\text{H}_2\text{O}$ (0.77 mmol), $\text{Fe}(\text{NO}_3)_3 \cdot 9\text{H}_2\text{O}$ (0.11 mmol), urea (4 mmol) and NH_4F in a beaker filled with 16 mL distilled water and stirring vigorously for 30 min, the metal ions interact through electrostatic interaction adsorbed on the surface of NaCNN sheets, then transfer the mixed solution to a 20 mL Teflon-lined autoclave at 120 °C for 6 h. After cooling to room temperature, the sample was washed several times with water and ethanol, and then dried in an oven overnight to obtain NiFe-LDH.

2.3. Synthesis of NaCNN/NiFe-LDH

A certain amount of NaCNN was added to the $\text{H}_2\text{O}/\text{CH}_3\text{OH}$ (1:3) mixture. After sonicating for 45 min, adding NiFe-LDH and stirring vigorously for 30 min, the metal ions were adsorbed on the surface of NaCNN sheets through electrostatic interaction. The product was washed with water and ethanol several times, and then dry overnight in an oven to obtain NaCNN/NiFe-LDH.

2.4. Synthesis of Ag/NaCNN/NiFe-LDH

The light deposition process was used to deposit Ag quantum dots on the surface of NaCNN/NiFe-LDH. Adding 0.4 g of NaCNN/NiFe-LDH to 200 mL of deionized water, stirred for 30 min, and then adding 1 mL of AgNO_3 (1 M), and irradiated with 500 W Xenon lamp for 30 min, washed with deionized water for several times, and put it in an oven at 50 °C to get ternary product Ag/NaCNN/NiFe-LDH.

3. Results and discussion

3.1. Morphology and structure

The crystal phase analysis of the prepared photocatalyst was carried out by X-ray diffraction (XRD). As shown in Fig. S1, the main characteristic diffraction peak of the original $\text{g-C}_3\text{N}_4$ is at $2\theta = 27.3^\circ$ [33], which corresponds to the (002) crystal plane of the hexagonal graphite carbonitride structure, reflecting the tri-s-triazine in-plane structural

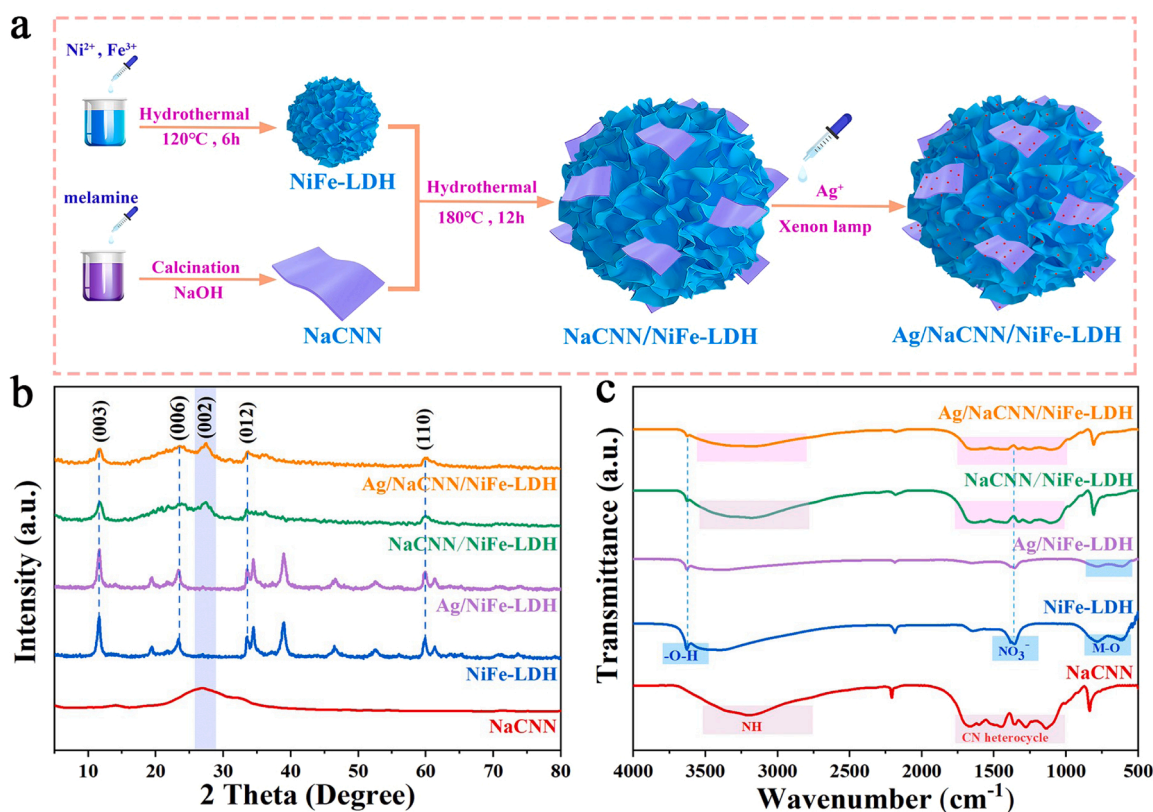


Fig. 1. Schematic diagram for preparation of three-dimensional flower-shaped Ag/NaCNN/NiFe-LDH heterostructures (a), typical XRD patterns (b), and FT-IR spectra (c) of different samples.

stacking of motifs and interlayer stacking of conjugating aromatic systems. Compared with pristine $\text{g-C}_3\text{N}_4$, the (002) peak width of CNN and NaCNN becomes larger, indicating the disorder of the structure. In addition, the (002) peak of NaCNN shifts from 27.3° to 27.8° [34], revealing a decrease in the stacking distance between layers due to the insertion of Na^+ into the heptazine-based melon framework. The reduction of the stacking distance is also related to the coordination of N or O atoms to enhance the interaction between adjacent layers. It is worth noting that the reduction of the stacking distance between layers is beneficial to the transfer of photogenerated charge carriers between adjacent layers.

Fig. 1b shows the typical characteristic diffraction peaks of NiFe-LDH at $2\theta = 11.6, 23.5, 33.4$ and 60° in the composite material, corresponding to the (003), (006), (009) and (110) crystal planes of NiFe-LDH, respectively [35,36]. The Ag/NaCNN/NiFe-LDH shows sharp characteristic peaks, indicating that NaCNN and Ag is successfully loaded on NiFe-LDH, but compared with the characteristic diffraction peaks of NiFe-LDH and NaCNN alone, the characteristic diffraction peaks is weakened, which may be related to the modification of the anions occupied by the NiFe-LDH layer. In addition, as a result of the low content of Ag, no characteristic peak of Ag is observed clearly.

As shown in Fig. S2, it is found that $\text{g-C}_3\text{N}_4$ and NaCNN emerge similar characteristic Fourier Transform Infrared Spectroscopy (FT-IR) bands. There is a feature extraction zone at 808 cm^{-1} with a seven-ring step curve, the signals corresponding to the typical -CN and -C=N tensile and flexural vibration modes appear in the region of $1000\text{--}1750\text{ cm}^{-1}$. NaCNN found a broad absorption band at $2500\text{--}3400\text{ cm}^{-1}$, which is due to the extension of -OH and acidic C-OH groups, the accumulation of adsorbed H_2O , and the extension of -NH and -NH_2 groups. It is worth noting that a new peak appears at 2178 cm^{-1} , which belongs to the tensile mode of cyano group ($\text{-C}\equiv\text{N}$), which proves that the cyano group function exists in the sample after the cyanamide

calcining, and the cyano group acts as a strong electron attractor group, and can promote the dissociation of electrons and holes [37,38]. Fig. 1c shows that the peak of NiFe-LDH at 1381 cm^{-1} may be related to the stretching vibration of NO_3^- . Its absorption band at $600\text{--}900\text{ cm}^{-1}$ is related to Fe-O, Ni-O and Ni-O-Fe, the metal-oxygen and metal-oxygen-metal lattice vibrations of NiFe-LDH [35]. The absorption band at 3700 cm^{-1} is an overlapping tensile shock belonging to the -O-H group. Since the content of Ag is low, no characteristic absorption peak of Ag is observed. In addition, in the infrared spectrum of the composite sample, the absorption bands at 1640 and 3153 cm^{-1} are the hydrogen bonds and water molecules (O-H) existing between NiFe-LDH and NaCNN. The above results further illustrate the successful combination of NiFe-LDH, NaCNN and Ag.

Scanning electron microscope (SEM) and transmission electron microscope (TEM) showed the morphological characteristics of Ag/NaCNN/NiFe-LDH. As shown in Fig. S3a, the NiFe-LDH has regularly distributed wrinkled and curled two-dimensional nanosheets. The thickness of the nanosheets is about 20 nm, and the lateral dimension is $\sim 100\text{--}200\text{ nm}$. The three-dimensional curd structure is composed of NiFe-LDH nanosheets stacked on each other, and the average curd width is about $1\text{ }\mu\text{m}$ (Fig. 2a). With the purpose of introducing alkali metal Na-doped defects on the original $\text{g-C}_3\text{N}_4$, a co-crystal ion heat treatment method of NaCl is used (Fig. S4). The presence of co-crystals promotes the mass transfer of the reactants and makes the alkali metal Na-doped defects becomes possible. Fig. 2b shows the two-dimensional sheet structure of NaCNN. The surface of the nanosheets is slightly rough, which may be caused by the etching of NaCl at high temperature, which corrodes the surface of NaCNN. Fig. 2c shows that NaCNN nanosheets are anchored on the surface of the curd of NiFe-LDH. These two layered structures can establish a good cooperative relationship through charge transfer or electrostatic interaction, which effectively enhances the utilization of light absorption and charge transfer. Through the TEM

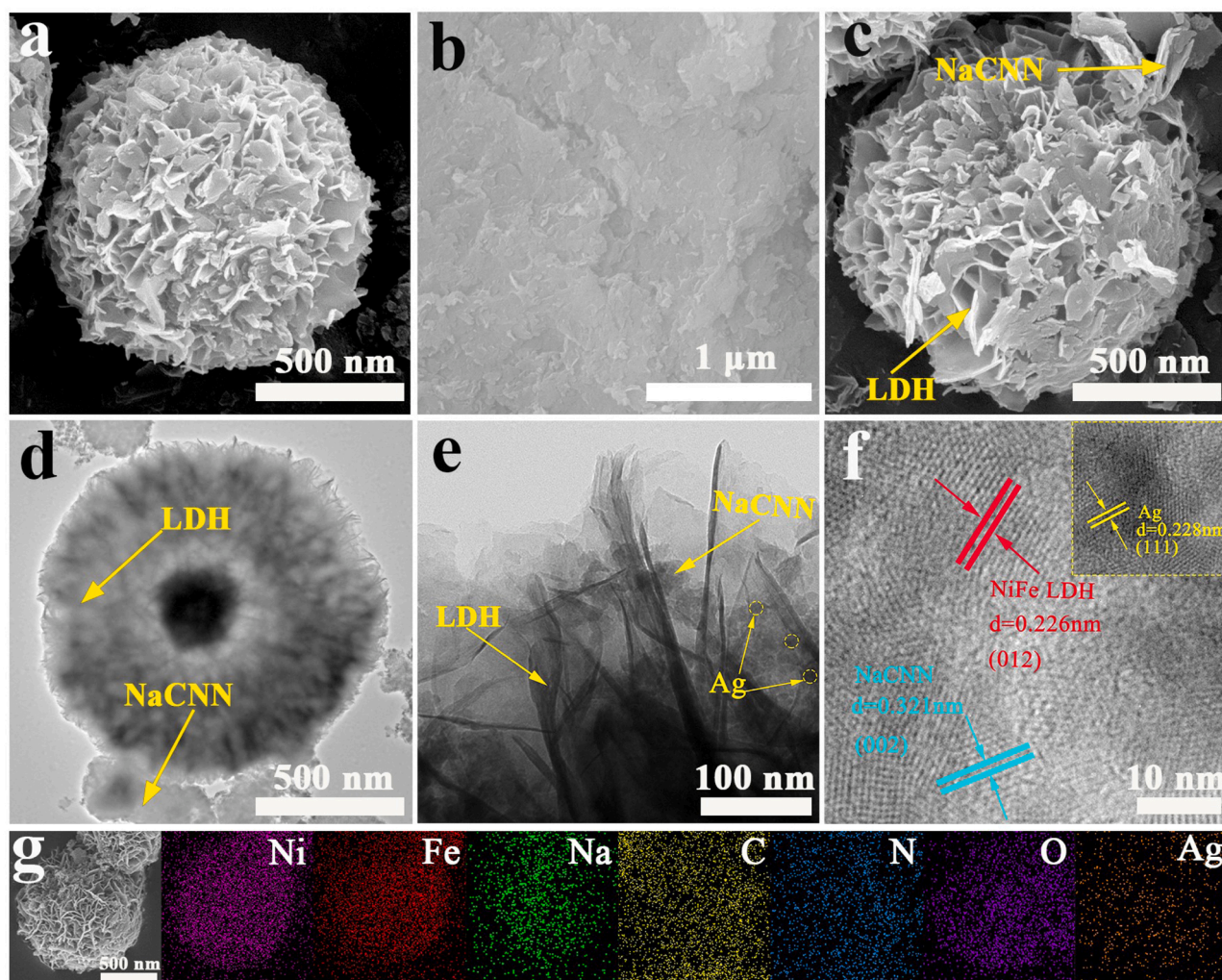


Fig. 2. SEM images of flower-shaped NiFe-LDH (a), NaCNN (b), Ag/NaCNN/NiFe-LDH (c), TEM images (d–f) and the element mappings (g) of Ag/NaCNN/NiFe-LDH.

image of Ag/NaCNN/NiFe-LDH (Fig. 2d), it can be seen that the nanosheets of NaCNN are successfully anchored on the curd of NiFe-LDH. In the process of stacking, the NiFe-LDH nanosheets are first stacked into a central sphere in the middle, and then the rest of the NiFe-LDH nanosheets grow evenly and dispersedly around the central body. It can be observed that the NiFe-LDH nanosheets in the center of the curd are most densely packed (Fig. S3b). The stacking of sheet-like structures can form voids, which is beneficial to increase the specific surface area of the catalyst. The specific surface area and pore structure of the sample are further studied by N_2 adsorption-desorption. As shown in Fig. S5, all samples are of type IV isotherm, indicating mesoporous structure. The Brunauer-Emmett-Teller (BET) specific surface area of $g\text{-C}_3\text{N}_4$ and NaCNN is 52.04 and $57.2\text{ m}^2\text{ g}^{-1}$. Compared with pure $g\text{-C}_3\text{N}_4$, the specific surface area of NaCNN is slightly increased [26]. Ag/ $g\text{-C}_3\text{N}_4$ /NiFe-LDH ($116.87\text{ m}^2\text{ g}^{-1}$) and Ag/NaCNN/NiFe-LDH ($120.4\text{ m}^2\text{ g}^{-1}$) are significantly higher than those of single materials. In Fig. 2e, it can be observed that Ag quantum dots and NaCNN are dispersed on the NiFe-LDH, which proves the successful recombination of the composite material. In the high-resolution TEM, the lattice fringes of the original $g\text{-C}_3\text{N}_4$ cannot be observed. On the contrary, NaCNN has obvious lattice fringes, indicating that NaCNN has good crystallinity. In addition, from Fig. 2f, it can be seen that the NiFe-LDH and NaCNN nanosheets and Ag quantum dots, the lattice spacing of the (111) crystallographic plane of the Ag quantum dots is 0.24 nm , the (002) crystallographic plane lattice spacing of NaCNN is 0.321 nm and the spacing between the (012) planes of NiFe-LDH is 0.226 nm . Fig. 2g analyzes the elements distribution of

Ag/NaCNN/NiFe-LDH, and the results show that Ni, Fe, C, N, O, Na and Ag are present in the catalyst uniformly, which proves the successful combination of Ag/NaCNN/NiFe-LDH.

To demonstrate the elemental composition of the photocatalyst, XPS analysis was performed on the composite material. As shown in Fig. 3a, the existence of Ni, Fe, C, N, O, Na and Ag can be seen through the XPS spectrum, proving the co-existence of NaCNN, NiFe-LDH and Ag. In order to further confirm the defects of alkali metal Na-doped $g\text{-C}_3\text{N}_4$, the XPS of $g\text{-C}_3\text{N}_4$, CNN and NaCNN are analyzed respectively.

It can be seen from Fig. S6 in the survey spectra of $g\text{-C}_3\text{N}_4$, CNN and NaCNN at 289, 400 and 534 eV, corresponding to the C 1s, N 1s and O 1s signals, respectively, while NaCNN displays a new peak at 1100 eV, which is attributed to the Na 1s signal. The peak of N 1s in the total XPS spectrum of CNN and NaCNN gradually decreases compare with that of pristine $g\text{-C}_3\text{N}_4$, indicating the formation of N-defects. In addition, NaCNN also shows the Na 1s spectrum, which can prove the alkali metal Na-doping. It can also be clearly seen from Table S1 that the N atom content in NaCNN has decreased, and the C/N atom ratio has increased from 1.9 to 6.8, and the Na atom content has increased from 0% to 1.26%, indicating the deficient of some N atoms and the doping of alkali metals Na. With the purpose of further clarify the types of N-deficient, a higher resolution N 1s spectrum is recorded. As shown in Fig. 3b, the N 1s spectrum of pure $g\text{-C}_3\text{N}_4$ has four peaks at 398.6, 399.6, 401.2 and 403.7 eV, respectively, corresponding to the double coordinated nitrogen atom ($\text{C}=\text{N}-\text{C}$), the third N atom (C_3-N), amino-functional group (C_2-NH) and π excited NH_x group [39]. From N 1s spectrum we can see

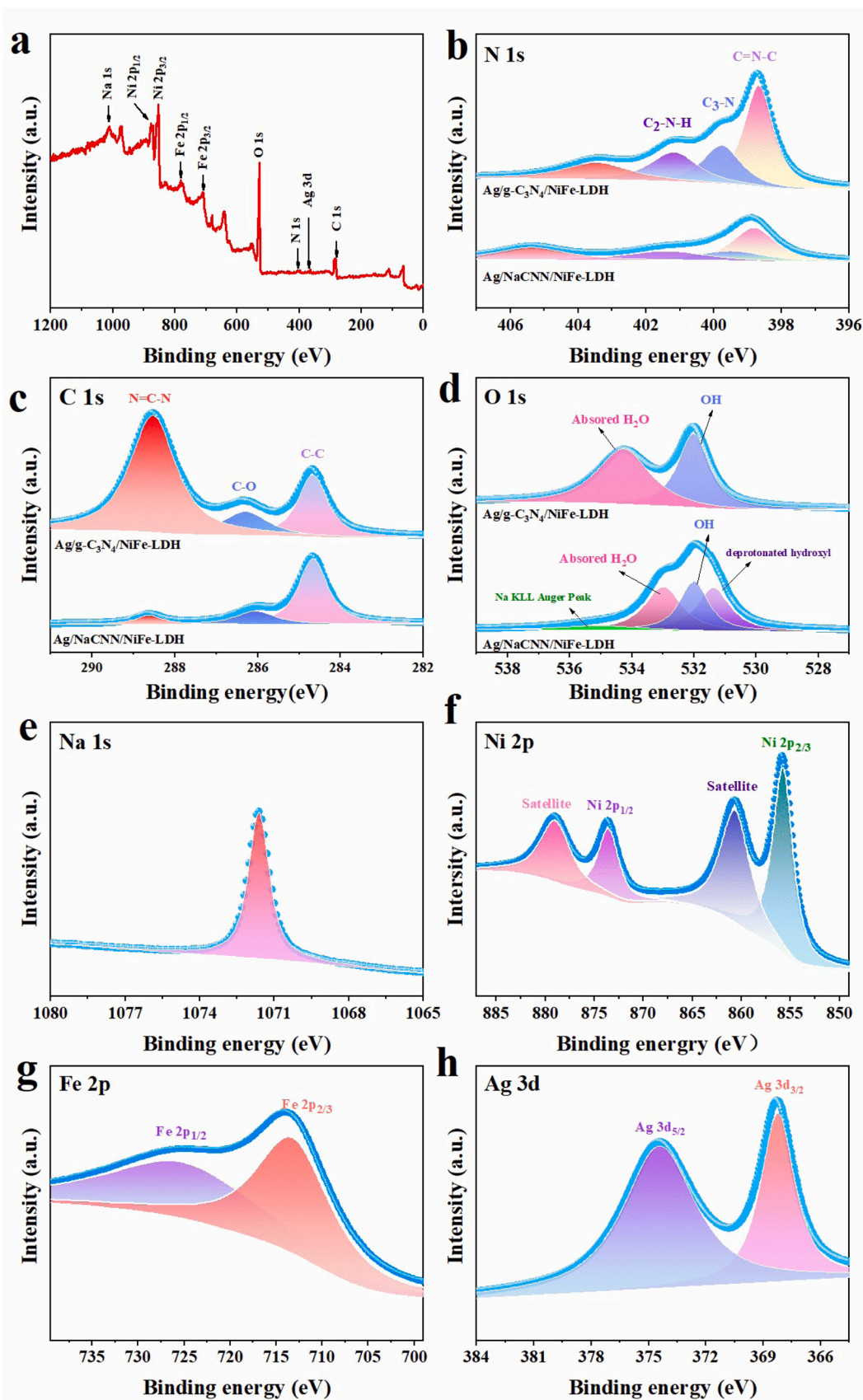


Fig. 3. XPS spectra of prepared: full survey of (a) Ag/NaCNN/NiFe-LDH, (b) N 1s, (c) C 1s, (d) O 1s, (e) Na 1s, (f) Ni 2p, (g) Fe 2p, (h) Ag 3d.

that the four peaks of the NaCNN spectrum are red-shifted compared with pristine $g\text{-C}_3\text{N}_4$, and the peaks are reduced, indicating the formation of N defects. These results indicate that in the co-crystallization process, part of $\text{C}=\text{N}-\text{C}$, C_3-N , C_2-NH is removed, resulting in the opening of N-deficient and s-triazine. The high-resolution spectra of C 1s of pure $g\text{-C}_3\text{N}_4$ showed (Fig. 3c) three peaks at 284.4, 286.15 and 288.2 eV, corresponding to sp^2 carbon ($\text{C}=\text{C}$), sp^3 carbon ($\text{C}-\text{O}$) and ($\text{N}=\text{C}-\text{N}$), respectively. In contrast, the peak of $\text{N}=\text{C}-\text{N}$ in the C 1s spectrogram of NaCNN is significantly weakened, indicating that the $\text{N}=\text{C}-\text{N}$ is weakened, fully indicating the formation of N-defects. In addition, the O 1s spectrum shows (Fig. 3d) that, the peak at 532.0 eV is attributed to the lattice oxygen and the peak at 534.5 eV is attributed to adsorbed water. Compared with pristine $g\text{-C}_3\text{N}_4$, NaCNN forms two new peaks [41]. The peak of NaCNN at 531.3 eV is due to the Na-KLL Auger peak due to alkali metal Na-doping, and the peak at 535.2 eV is due to the substitution of protons by alkali metal cations to produce deprotonated hydroxyl groups ($-\text{O}-$) [34]. Fig. 3e shows that the XPS spectrum of Na 1s shows a peak at 1071.9 eV, which proves the successful doping of Na. In order to prove the existence of Na, the high-resolution spectrum of Cl 2p is analyzed (Fig. S7), and it is found that it did not have any peaks, indicating the efficient Na doping in NaCNN. The above results indicate the successful Na-doping and the formation of N-defects in NaCNN. The

XPS of Ni 2p (Fig. 3f) shows that there are two main peaks at 873.5 and 855.6 eV, which are attributed to Ni $2p_{1/2}$ and Ni $2p_{3/2}$ with the valence of + 2, respectively, and at 873.6 and 855.6 eV, there are two satellite peaks [40,42]. The high-resolution spectrum of Fe 2p shows that there are two peaks at 712 and 723.5 eV (Fig. 3g), corresponding to Fe $2p_{3/2}$ and Fe $2p_{1/2}$ with valence states of + 3 [43]. In the XPS spectrum of Ag (Figs. 3h), 368.1 and 374.1 eV are attributed to Ag $3d_{3/2}$ and Ag $3d_{5/2}$, respectively [44]. The bonding energy difference between them are 6 eV, which is characteristic of its spin-orbit separation, indicating the formation of metal Ag in Ag/NaCNN/NiFe-LDH.

3.2. Photothermal and optical properties

The photothermal effect is also an important factor that affects the photocatalytic activity. The infrared thermal driver is used to measure and study the photothermal effect of the photocatalyst. At the initial temperature of 25 °C, the core temperature of the NiFe-LDH increased from 52.7° to 87.2°C under simulated sunlight for 120 s (Fig. 4a). The core temperature of Ag/NaCNN/NiFe-LDH increases from 58.1° to 115.7°C (Fig. 4b), which is about 30 °C higher than that of NiFe-LDH alone. Compared with pure NiFe-LDH, NaCNN/NiFe-LDH and Ag/NiFe-LDH have higher photothermal properties (Fig. S8), indicating

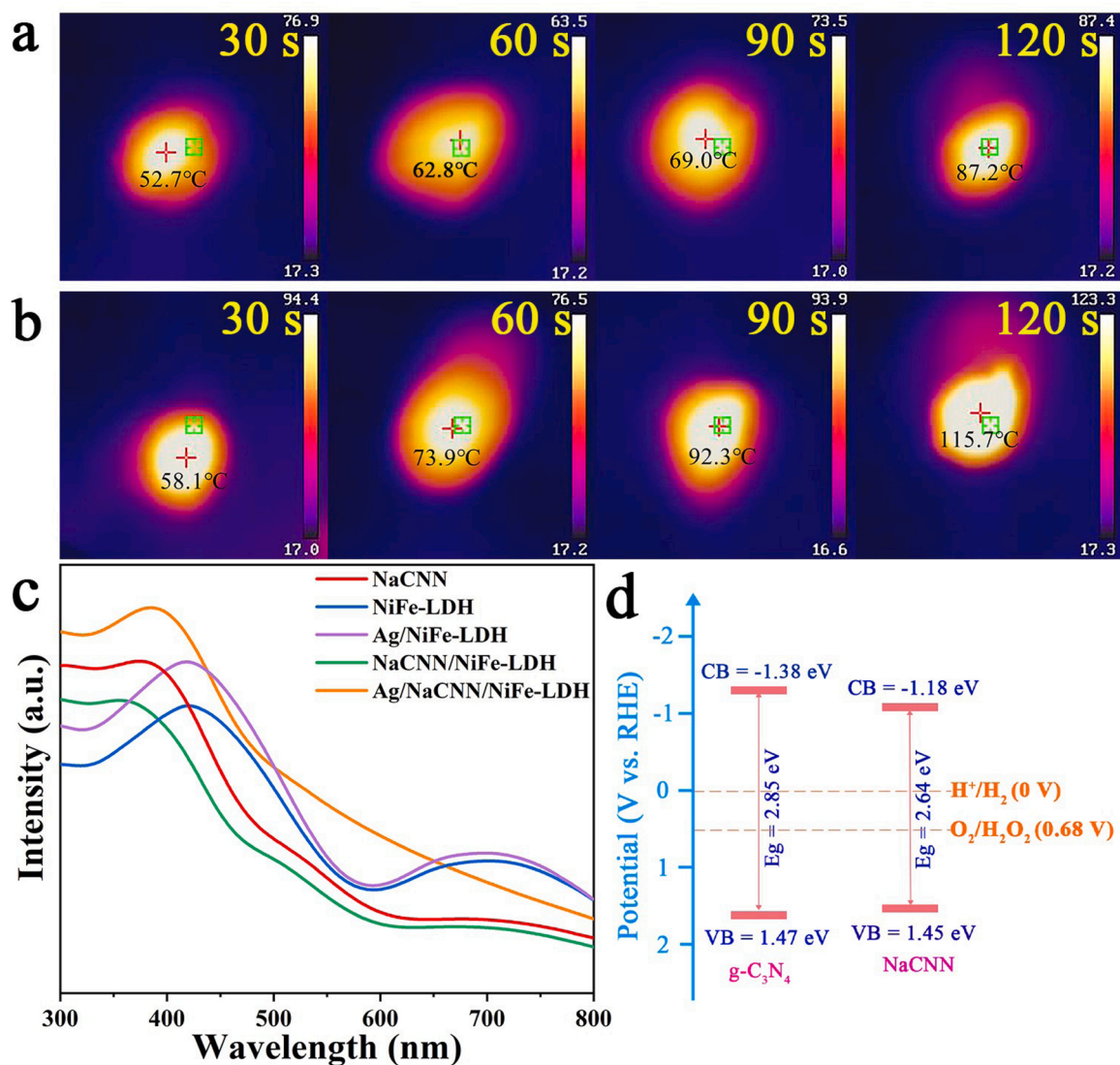


Fig. 4. Infrared photographs of NiFe-LDH and Ag/NaCNN/NiFe-LDH with the starting temperature of 25 °C (a-b), the UV-vis diffuse reflectance absorption spectra (c), Schematic illustration of the band gap alignment of $g\text{-C}_3\text{N}_4$ and NaCNN (d).

that the SPR effect of Ag and defective NaCNN can improve the photothermal performance of the catalyst obviously. The ‘hot electrons’ excited due to the SPR effect of Ag can be transferred from the surface of the metal quantum dots to NiFe-LDH, thereby facilitating the separation of photogenerated carriers. Compared with pure NiFe-LDH, the ternary composite has a significant photothermal effect. Good photothermal properties can accelerate the migration of photogenerated carriers, which facilitates the separation of electrons and holes and thus accelerates the production of hydrogen. In addition, it can also introduce infrared light into the photocatalytic process to provide the driving force for the separation of photogenerated carriers and increase the migration rate of electrons, thus improving photocatalytic performance.

As shown in Fig. 4c, the absorption edge of NiFe-LDH is about 522 nm [45,46], the absorption edge of Ag/NaCNN/NiFe-LDH is red-shifted, compared with pristine NiFe-LDH, indicating the light absorption capacity significantly improved [24]. When there is a significant red shift along the absorption edge of Na embedded (Fig. S9), NaCNN will widen the absorption edge to 500 nm, while the absorption edge of pristine g-C₃N₄ is at 450 nm, which may be attributed to the narrowing of the band gap caused by the Na-doping in NaCNN and the introduction of N-defects. The band gap variation of all samples is further explained and the band gap of the catalyst is obtained by calculating (Fig. S10). The band gaps of g-C₃N₄, NaCNN, NiFe-LDH, Ag/NiFe-LDH, NaCNN/NiFe-LDH, Ag/NaCNN/NiFe-LDH are 2.70, 2.64, 2.20, 2.42, 2.18 and 2.03 eV, respectively. The results show that as shown in Fig. 4d, compare with the original g-C₃N₄, the conduction band position of NaCNN has dropped from −1.41 to −1.18 eV, while the valence band position has not changed significantly [26]. However, the conduction band position of NaCNN is more negative than the potential value of O₂ reduction to H₂O₂. The bit (0.68 eV) is more negative, which

also illustrates the feasibility of NaCNN for H₂O₂ production.

3.3. Photoelectrochemical properties

A series of experiments were conducted to demonstrate the charge separation and transfer of the obtained samples. The light-induced electron-hole recombination rate was revealed by steady-state photoluminescence (SS-PL) spectroscopy. As shown in the plot of Fig. 5a, Ag/NaCNN/NiFe-LDH exhibits the lowest SS-PL intensity compared with NiFe-LDH and NaCNN/NiFe-LDH, indicating a lower recombination rate and longer carrier lifetime of photogenerated carriers. In addition, the lifetimes of photogenerated carriers were detected by transient PL decay curves (Fig. 5b), and the emission decay curves of the photocatalysts are fitted by double exponential kinetic functions. The average lifetime τ of the photocatalyst is obtained by the following equation:

$$\tau = (B_1\tau_1^2 + B_2\tau_2^2) / (B_1\tau_1 + B_2\tau_2) \quad (1)$$

The average PL lifetimes of NiFe-LDH, NaCNN/NiFe-LDH, and Ag/NaCNN/NiFe-LDH are 2.26, 2.41, and 2.87 ns, respectively. The results show that the carrier lifetime of Ag/NaCNN/NiFe-LDH is the longest among all samples. The increase of photogenerated carrier lifetime can effectively improve the utilization of photoinduced carriers. Fig. 5c shows that compared with NiFe-LDH, NaCNN/NiFe-LDH and Ag/NaCNN/NiFe-LDH composite material shows a higher photocurrent intensity, indicating the transmission of photogenerated electron carriers and separation is optimized.

From electrochemical impedance spectroscopy (EIS), as shown in Fig. S11, the ternary composite material Ag/NaCNN/NiFe-LDH ternary composite material has the smallest radius and the lowest electrochemical impedance, indicating that the resistance to the charge

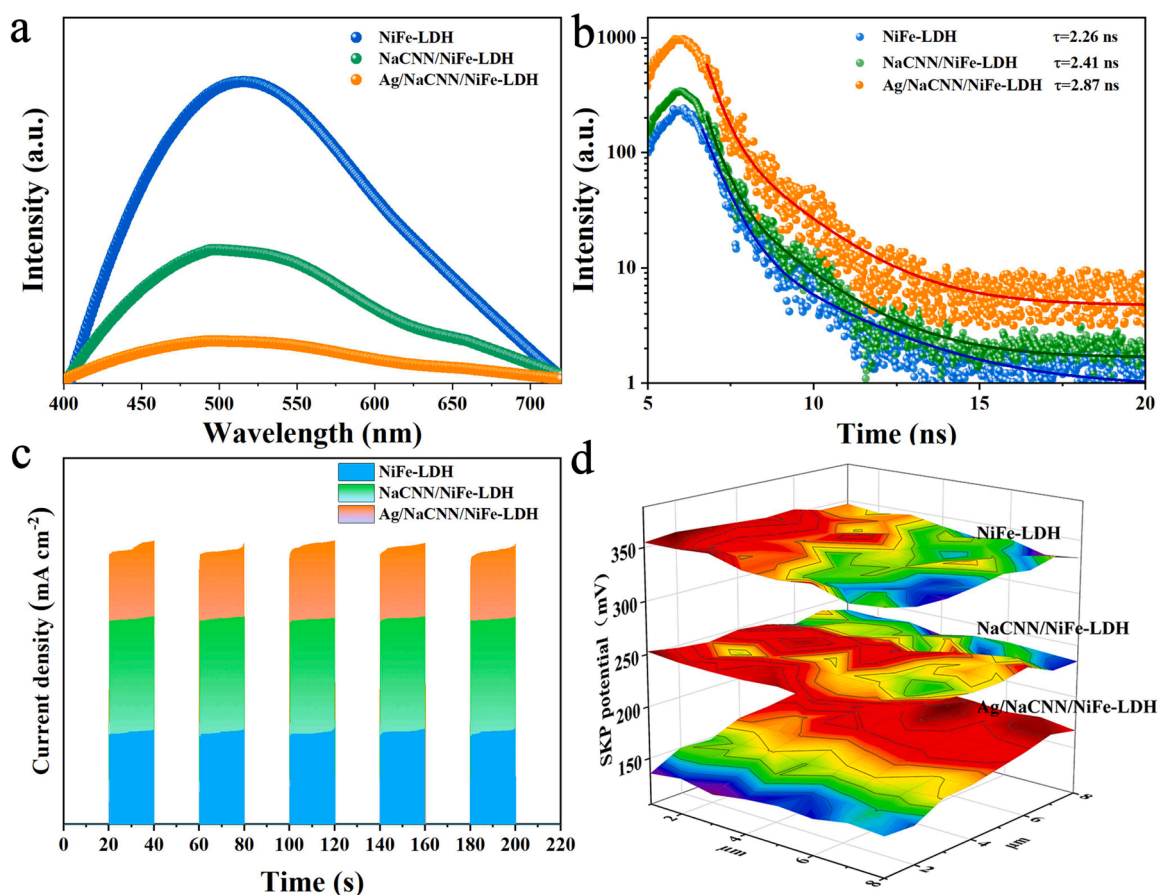


Fig. 5. Steady-state PL spectra (a), transient-state PL spectra (b), transient photocurrent responses (c), and scanning Kelvin probe maps (d) of NiFe-LDH, NaCNN/NiFe-LDH and Ag/NaCNN/NiFe-LDH.

movement is low and promotes photogenerated charge transfer. The Scanning Kelvin Probe (SKP) test is used to check the work function of the sample. As shown in Fig. 5d, the work function of Ag/NaCNN/NiFe-LDH is the lowest, indicating that the Ag/NaCNN/NiFe-LDH composite material is beneficial to electron escape and separation. According to the results of Mott-Schottky (Fig. S12), the flat band potential values of g-C₃N₄, CNN and NaCNN are -2.2 , -2.32 and -2.44 eV, respectively, and the band gaps can be obtained by calculation. NiFe-LDH flat band potential value is -1.4 eV [47]. Since the photoresponse of NiFe-LDH is lower than that of NaCNN, the photoresponse effect is obviously enhanced after introducing NaCNN and Ag.

3.4. Photocatalytic-Fenton activity and hydrogen production

As shown in Fig. 6a, the experiment to determine the photocatalytic degradation performance of the optimal pH shows that in the range of pH = 5–11, under all other conditions unchanged, Ag/NaCNN/NiFe-LDH shows the best degradation performance of 4-NPs under the condition of pH = 11, about 99% of 4-NPs is degraded within 120 min irradiation. Meanwhile, the relevant pseudo first-order kinetic fitting curves and apparent rate constants of Ag/NaCNN/NiFe-LDH degradation of 4-NPs at different pH are shown in Fig. S13. The degradation ability of Ag/NaCNN(5%)/NiFe-LDH, Ag/NaCNN(10%)/NiFe-LDH and Ag/NaCNN(15%)/NiFe-LDH for 4-NPs is compared considering the

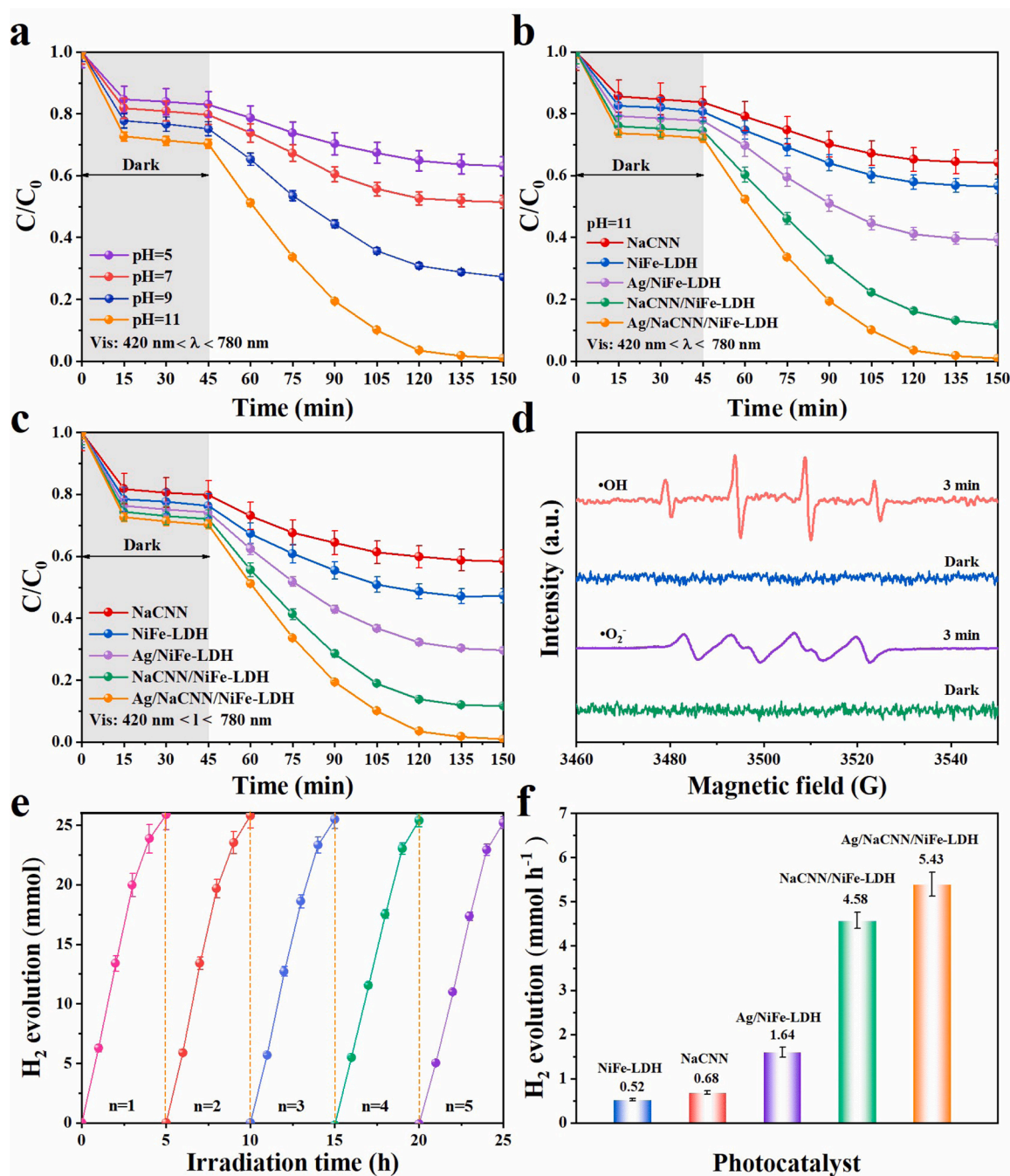


Fig. 6. Photocatalytic-Fenton degradation performance 4-NPs under visible light irradiation for Ag/NaCNN/NiFe-LDH at different pH (a), and different samples (b), photocatalytic-Fenton degradation performance of BPA under visible-light (c). ESR spectra of DMPO-•OH and DMPO-•O₂⁻ (d), the H₂ evolution cycles of NiFe-LDH/NaCNN/Ag for 25 h (e), and H₂ evolution (f) for different samples. (The error estimate was repeated five times).

effect of the ratio of the composites on the photocatalytic performance (Fig. S14). The experimental results showed that Ag/NaCNN(10%)/NiFe-LDH has the best degradation effect. The excellent photocatalytic performance is attributed to the effective acceleration of photo-generated electron-hole separation and the faster migration rate of photogenerated carriers by the composite. However, when the content of NaCNN is too high, it affects the size and thickness of the NiFe-LDH layered structure and hinders the transport of photogenerated electrons. In summary, the optimum pH = 11 and the content of NaCNN in the composite material of 10% are selected for other degradation evaluations.

Under pH = 11 and visible light irradiation (Fig. 6b), the degradation rate of 4-NPs by NiFe-LDH and Ag/NiFe-LDH is 40% and 60%, the degradation rate of Ag/NaCNN/NiFe-LDH exceeds 99%, and its apparent reaction rate constant is $4.32 \times 10^{-2} \text{ min}^{-1}$, which is compared with the single NiFe-LDH material ($k = 2.92 \times 10^{-3} \text{ min}^{-1}$) and the binary material NaCNN/NiFe-LDH ($k = 1.92 \times 10^{-2} \text{ min}^{-1}$) enhances by 2–14 times (Fig. S15). The degradation performance of Ag/NaCNN/NiFe-LDH composite material shows better performance than NiFe-LDH and NaCNN/NiFe-LDH. In order to prove the stability of the photocatalyst, the photocatalytic degradation cycle test is carried out on the composite material. After 7 recycles, the degradation rate of the composite material nearly remains unchanged, indicating the high stability (Fig. S16). After replacing the organic pollutant with BPA (Fig. 6c), it can be observed that its degradation efficiency can be up to 99% within 135 min, and its rate reaction constant is $4.325 \times 10^{-2} \text{ min}^{-1}$, which is about 15 times higher than that of NiFe-LDH ($k = 2.92 \times 10^{-3} \text{ min}^{-1}$) (Fig. S17) and higher than literatures (Table S2). In addition, the Ag/NaCNN/NiFe-LDH is prepared in Fig. S18 has excellent photocatalytic performance against other pollutants such as MO, MB, Phenol, 2,4-DCP and RhB, and all have been exposed to visible light within 115 min and up to 94–99% degradation rate. The excellent photocatalytic degradation performance of Ag/NaCNN/NiFe-LDH photocatalyst may be attributed to the generation of a large number of $\bullet\text{OH}$. In addition, the porosity of the material can also improve the degradation performance of the photocatalyst, the specific surface area and pore structure of the sample is studied through the N_2 adsorption-desorption isotherm. The pore size distribution determines from the desorption branch by the BJH method shows that the pore size of the composite material is mainly concentrated at 2–25 nm, while the pore size of NaCNN is mainly concentrated at 2–10 nm, and the pore size distribution of pristine $\text{g-C}_3\text{N}_4$ is wider (Fig. S19). The above results indicate the stable photocatalytic performance of Ag/NaCNN/NiFe-LDH to degrade pollutants. The reason for the enhanced photocatalytic performance of the ternary composite may be ascribed to the special structure favoring the generation of a large number of hydroxyl radicals. To consider whether the introduction of Cl would affect the performance of the catalyst, comparative experiments are performed for Ag/ $\text{g-C}_3\text{N}_4$ /NiFe-LDH and Ag/NaCNN/NiFe-LDH under the same conditions (Fig. S20). The results show that the degradation rate of Ag/ $\text{g-C}_3\text{N}_4$ /NiFe-LDH is lower than that of Ag/NaCNN/NiFe-LDH under visible light irradiation for 150 min, so that the negative effect of Cl on the catalyst could be excluded. In addition, NaOH and $\text{Na}_5\text{P}_3\text{O}_{10}$ are used as the introduction agents for Na-doped (denoted as Ag/NaCNN-OH/NiFe-LDH and Ag/NaCNN- P_3O_{10} /NiFe-LDH) and their degradation properties were analyzed comparatively (Fig. S21), and the experimental results show that the composites obtained by doping with NaCl are more efficient in degrading 4-NPs. To further determine the stability of Ag/NaCNN/NiFe-LDH, the samples before and after the cyclic reaction were compared by XRD (Fig. S22), XPS (Fig. S23), UV-Vis (Fig. S24) and FT-IR (Fig. S25), respectively. The results show no significant changes in the diffraction peaks of XRD, XPS characteristic peaks, UV-Vis absorption wavelength and FT-IR characteristic peaks, which further confirmed the high stability of Ag/NaCNN/NiFe-LDH.

The photochemical properties of the composite material are measured by the terephthalic acid fluorescence method (FL). Because

terephthalic acid (PTA) can react with $\bullet\text{OH}$ (Fig. S26), it can produce 2-hydroxyterephthalic acid, a product with strong fluorescence, which can be used to measure the content of hydroxyl radicals. The results show that Ag/NaCNN/NiFe-LDH has the highest fluorescence intensity among all materials, which proves that the Z-scheme heterojunction of the composite material is beneficial to the generation of $\bullet\text{OH}$, and further shows that the separation rate of photogenerated carriers is improved.

The 5,5-dimethyl-1-pyrroline N-oxide (DMPO) is used as a trapping agent in the photocatalytic process by electron spin resonance (ESR) experiments. As can be seen in Fig. 6d, no signals corresponding to DMPO- $\bullet\text{OH}$ and DMPO- $\bullet\text{O}_2^-$ are detected under dark conditions, indicating that no photoreaction occurred. Under light conditions, the detected DMPO- $\bullet\text{OH}$ signal response is more pronounced, and four peaks with 1:2:2:1 line spectrum intensity are detected, indicating the production of $\bullet\text{OH}$ during the photocatalytic reaction. For DMPO- $\bullet\text{O}_2^-$, four characteristic peaks with typical signals of 1:1:1:1 intensity were detected, which also proved the generation of $\bullet\text{O}_2^-$ in the system. To further demonstrate the degradation mechanism of organic pollutants by reactive substances, the main reactive groups in the reaction process were identified by capture experiments, adding isopropyl alcohol (IPA), ethylenediaminetetraacetic acid (EDTA-Na), p-benzoquinone (BQ) and AgNO_3 to capture $\bullet\text{OH}$, h^+ , $\bullet\text{O}_2^-$ and e^- . As shown in Fig. S27, the degradation rates of Ag/NaCNN/NiFe-LDH are affected by the addition of IPA and EDTA-Na to the system to different degrees, indicating that both $\bullet\text{OH}$ and h^+ are involved in the reaction during the degradation of pollutants, and the effect of $\bullet\text{OH}$ on the catalytic activity is better than that of h^+ . When BQ is added, it has little effect on the degradation rate, indicating that $\bullet\text{O}_2^-$ produced by the photocatalyst plays a little role in the photocatalytic reaction process. This is consistent with the results of ESR, indicating that $\bullet\text{OH}$ plays a dominant role in the photocatalytic degradation process.

To further verify the photocatalytic efficiency, the Ag/NaCNN/NiFe-LDH photocatalyst was subjected to a cycle stability test (Fig. 6e). After seven cycles, although the hydrogen production rate decreased slightly, it still shows excellent stability. Fig. 6f shows the hydrogen production efficiency of NaCNN, NiFe-LDH, NaCNN/NiFe-LDH and Ag/NaCNN/NiFe-LDH photocatalysts under visible light irradiation. It can be seen that the maximum hydrogen production of Ag/NaCNN/NiFe-LDH is as high as $0.543 \text{ mmol h}^{-1}$, which is about 10 times higher than that of pristine NiFe-LDH. The excellent photocatalytic hydrogen evolution could be ascribed to the efficient spatial charge separation of this special Z-scheme heterojunction.

3.5. Photocatalytic mechanism analysis

To illustrate the electron transfer pathway, DMOP- $\bullet\text{OH}$ and DMOP- $\bullet\text{O}_2^-$ were detected in the samples by ESR detection analysis (Fig. S28). For the original NaCNN, no DMOP- $\bullet\text{OH}$ signal is detected because the standard reduction potential of $\text{H}_2\text{O}/\bullet\text{OH}$ is 1.99 eV vs NHE and the positive E_{VB} value of NaCNN cannot oxidize H_2O to $\bullet\text{OH}$. In addition, only the signals of DMOP- $\bullet\text{OH}$ were detected for NiFe-LDH and Ag/NiFe-LDH because the negative value of the E_{CB} of NiFe-LDH was not sufficient to reduce O_2 to $\bullet\text{O}_2^-$. While NaCNN/NiFe-LDH and Ag/NaCNN/NiFe-LDH can detect DMOP- $\bullet\text{OH}$ and DMOP- $\bullet\text{O}_2^-$ signals. The above results reasonably exclude the possibility of Ag/NaCNN/NiFe-LDH forming a conventional type II heterojunction. If the photo-induced holes of NiFe-LDH aggregate to the valence band of NaCNN, it contradicts the results of ESR. Taken together, this suggests that Z-scheme heterojunction rather than type II heterojunction are formed between the composites.

Through the above characterization and performance testing, the photocatalytic reaction mechanism can be further proposed. As shown in Fig. 7, the band gaps of NiFe-LDH and NaCNN are estimated to be ~ 2.20 and 2.64 eV, respectively. The charge transfer method between NiFe-LDH, NaCNN and Ag should conform to the Z-scheme heterojunction. The conduction band position of NiFe-LDH ($\text{CB} = 0.59 \text{ eV}$) is

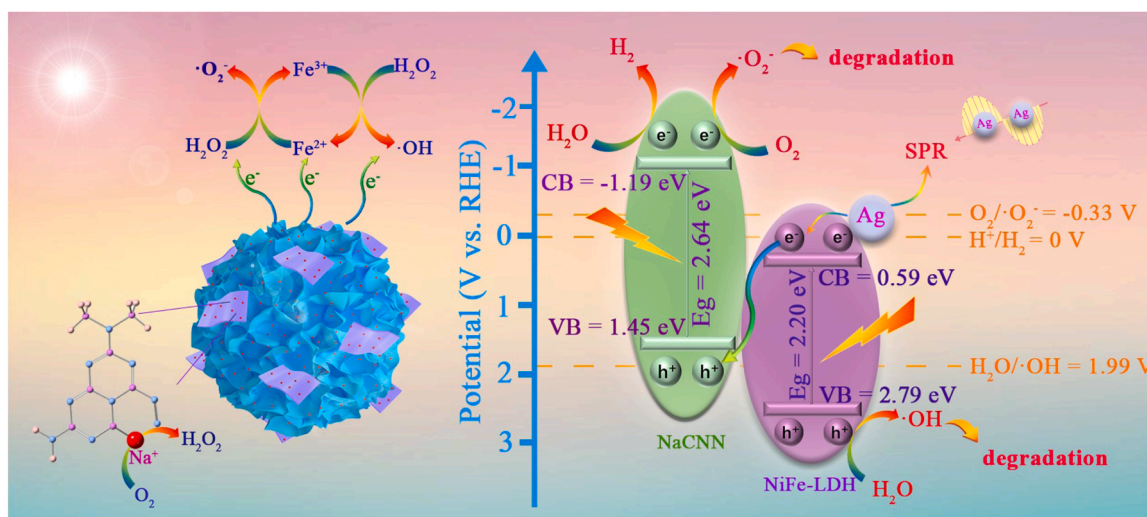
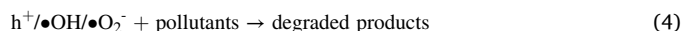
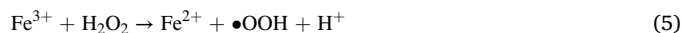


Fig. 7. Schematic diagram of the photocatalytic mechanism of Ag/NaCNN/NiFe-LDH Z-scheme heterojunction under visible light irradiation.

lower than that of NaCNN (CB = −1.19 eV), but the valence band position of NiFe-LDH (VB = 2.79 eV) is significantly higher than that of NaCNN (VB = 1.45 eV). The photogenerated electrons are transferred from the conduction band of NiFe-LDH to the valence band of NaCNN, and then the holes of NaCNN recombine with the electrons of NiFe-LDH, and the photogenerated electrons finally gather on the CB of NaCNN. The photogenerated holes retained in the VB of NiFe-LDH are formed with sufficient energy to oxidize H₂O to produce •OH or directly participate in the degradation of pollutants, and the produced •OH can also participate in the removal of pollutants. Meanwhile, the electrons generated by light accumulate on the CB of NaCNN, and the gathered electrons not only reduce O₂ to •O₂[−], thus degrading pollutants, but also react with H⁺ to produce hydrogen gas [48,49]. Due to the doping of alkali metals Na and the construction of Z-scheme heterojunction, the SPR effect of Ag and the large specific surface area, the photocatalytic hydrogen production of Ag/NaCNN/NiFe-LDH is promoted obviously, which favors the practical application. As 'hot electrons', Ag quantum dots can promote the separation of photogenerated electron-hole pairs, broaden the light absorption range, increase light scattering, and improve the light-to-heat conversion rate of Ag/NaCNN/NiFe-LDH. These factors all facilitate to enhance the final photocatalytic performance. The reaction equation of the photocatalytic process is as follows:



Another important aspect of the resulting Ag/NaCNN/NiFe-LDH is the production of H₂O₂. The reason for H₂O₂ being generated can be attributed to the following reasons. The ability of the composite material to generate •OH radicals, which are generated in the photocatalytic-Fenton and photocatalytic reactions and play a synergistic role in degrading pollutants. In the photocatalytic-Fenton reaction, photogenerated carriers promote the reduction of Fe³⁺ to Fe²⁺, and Fe³⁺ reacts with H₂O₂ to generate •OOH. Then, H₂O₂ oxidizes Fe²⁺ to Fe³⁺, generating •OH. In the photocatalytic-Fenton process, e[−] can produce •OH and •O₂[−], which can increase the number of free radicals and improve the photocatalytic activity. The photocatalytic-Fenton mechanism is as follows:



In addition, NaCNN can also produce H₂O₂ by photocatalysis.

According to literatures, under visible light irradiation ($\lambda > 420$ nm), pure g-C₃N₄, CNN and NaCNN produce H₂O₂ at concentrations of 53 μM, 2.1 mM and 4.8 mM within 60 min illumination [26]. The results show that the introduction of Na-doped defects can enhance light absorption so that electrons and holes can be quickly separated. Therefore, the Ag/NaCNN/NiFe-LDH Z-scheme favors the spatial charge separation and enhanced the production of H₂O₂, which promote the subsequent photocatalytic reaction and photocatalytic-Fenton reaction. The novel Z-scheme heterojunctions will have potential applications in fields of energy and environment.

4. Conclusions

In summary, we have demonstrated the fabrication of Ag/NaCNN/NiFe-LDH Z-scheme heterojunction via hydrothermal and calcination method. It exhibited excellent photocatalytic-Fenton performance in the degradation of 4-NPs, BPA, Phenol, and other pollutants, under the irradiation of visible light, in which the degradation rate of 4-NPs was up to 98%, and the hydrogen production rate was about 0.543 mmol h^{−1}. The improved photocatalyst performance could be attributed to the following reasons: (1) The introduction of Na-doped defects changes the band structure of NaCNN and narrows the band gap, which increases the separation and transfer rate of electrons and holes. (2) The bulbous structure of Ag/NaCNN/NiFe-LDH increases the specific surface area (120.4 m² g^{−1}). The flower-shaped structure exposed abundant active sites, which utilized the reflection and scattering of sunlight to enhance the utilization rate of light and enhanced the photocatalytic activity. (3) The Z-scheme heterojunction formed by Ag/NaCNN/NiFe-LDH combined with the synergy of the photocatalytic-Fenton reaction and the SPR effect effectively improved the degradation of pollutants and photothermal performance.

CRediT authorship contribution statement

Weifeng Kong: Data curation, Investigation, Writing – original draft, Methodology. **Zipeng Xing:** Methodology, Funding acquisition, Writing – review & editing. **Bin Fang:** Methodology, Visualization, Writing – review & editing. **Yongqian Cui:** Visualization, Writing – review & editing. **Zhenzi Li:** Writing – review & editing. **Wei Zhou:** Writing – review & editing, Funding acquisition.

Declaration of Competing Interest

The authors declare that they have no known competing financial

interests or personal relationships that could have appeared to influence the work reported in this paper.

Acknowledgments

We gratefully acknowledge the support of this research by the National Natural Science Foundation of China (21871078, 52172206), the Natural Science Foundation of Heilongjiang Province (JQ2019B001), the Natural Science Foundation of Shandong Province (ZR2021MB016), the Heilongjiang Postdoctoral Startup Fund (LBH-Q14135), the Heilongjiang University Science Fund for Distinguished Young Scholars (JCL201802), and the Heilongjiang Touyan Innovation Team Program.

Appendix A. Supporting information

Supplementary data associated with this article can be found in the online version at [doi:10.1016/j.apcatb.2021.120969](https://doi.org/10.1016/j.apcatb.2021.120969).

References

- [1] N. Uddin, H. Zhang, Y. Du, G. Jia, S. Wang, Z. Yin, Structural-phase catalytic redox reactions in energy and environmental applications, *Adv. Mater.* 32 (2020), 1905739, <https://doi.org/10.1002/adma.201905739>.
- [2] G.H. Jeong, S.P. Sasikala, T. Yun, G.Y. Lee, W.J. Lee, S.O. Kim, Nanoscale assembly of 2d materials for energy and environmental applications, *Adv. Mater.* 32 (2020), 1907006, <https://doi.org/10.1002/adma.201907006>.
- [3] W. Wang, C. Deng, S. Xie, Y. Li, W. Zhang, H. Sheng, C. Chen, J. Zhao, Photocatalytic c-c coupling from carbon dioxide reduction on copper oxide with mixed-valence copper(I)/copper(II), *J. Am. Chem. Soc.* 143 (2021) 2984–2993, <https://doi.org/10.1021/jacs.1c00206>.
- [4] X. Qiu, Y. Zhang, Y. Zhu, C. Long, L. Su, S. Liu, Z. Tang, Applications of nanomaterials in asymmetric photocatalysis: Recent progress, challenges, and opportunities, *Adv. Mater.* 33 (2021), 2001731, <https://doi.org/10.1002/adma.202001731>.
- [5] Q. Guo, C. Zhou, Z. Ma, X. Yang, Fundamentals of TiO₂ photocatalysis: concepts, mechanisms, and challenges, *Adv. Mater.* 31 (2019), 1901997, <https://doi.org/10.1002/adma.201901997>.
- [6] G. Zhao, W. Ma, X. Wang, Y. Xing, S. Hao, X. Xu, Self-water-absorption-type two-dimensional composite photocatalyst with high-efficiency water absorption and overall water-splitting performance, *Adv. Powder Mater.* (2021), <https://doi.org/10.1016/j.apmater.2021.09.008>.
- [7] S. Song, J. Qu, P. Han, M.J. Hülsey, G. Zhang, Y. Wang, S. Wang, D. Chen, J. Lu, N. Yan, Visible-light-driven amino acids production from biomass-based feedstocks over ultrathin cds nanosheets, *Nat. Commun.* 11 (2020) 4899, <https://doi.org/10.1038/s41467-020-18532-3>.
- [8] J. Zhang, J. Liu, L. Xi, Y. Yu, N. Chen, S. Sun, W. Wang, K.M. Lange, B. Zhang, Single-atom Au/NiFe layered double hydroxide electrocatalyst: probing the origin of activity for oxygen evolution reaction, *J. Am. Chem. Soc.* 140 (2018) 3876–3879, <https://doi.org/10.1021/jacs.8b00752>.
- [9] L. Yu, J.F. Yang, B.Y. Guan, Y. Lu, X.W.D. Lou, Hierarchical hollow nanoprisms based on ultrathin Ni-Fe layered double hydroxide nanosheets with enhanced electrocatalytic activity towards oxygen evolution, *Angew. Chem. Int. Ed.* 57 (2018) 172–176, <https://doi.org/10.1002/anie.201710877>.
- [10] P.S. Li, X.X. Duan, Y. Kuang, Y.P. Li, G.X. Zhang, W. Liu, X.M. Sun, Tuning electronic structure of NiFe layered double hydroxides with vanadium doping toward high efficient electrocatalytic water oxidation, *Adv. Energy Mater.* 8 (2018), 1703341, <https://doi.org/10.1002/aenm.201703341>.
- [11] W.D. Zhang, Q.T. Hu, L.L. Wang, J. Gao, H.Y. Zhu, X.D. Yan, Z.G. Gu, In-situ generated Ni-MOF/LDH heterostructures with abundant phase interfaces for enhanced oxygen evolution reaction, *Appl. Catal. B* 286 (2021), 119906, <https://doi.org/10.1016/j.apcatb.2021.119906>.
- [12] Y. Zhao, L. Zheng, R. Shi, S. Zhang, X. Bian, F. Wu, X. Cao, G.I.N. Waterhouse, T. Zhang, Alkali etching of layered double hydroxide nanosheets for enhanced photocatalytic N₂ reduction to NH₃, *Adv. Energy Mater.* 10 (2020), 2002199, <https://doi.org/10.1002/aenm.202002199>.
- [13] S. Zhang, Y. Zhao, R. Shi, C. Zhou, G.I.N. Waterhouse, Z. Wang, Y. Weng, T. Zhang, Sub-3 nm ultrafine Cu₂O for visible light driven nitrogen fixation, *Angew. Chem. Int. Ed.* 60 (2021) 2554–2560, <https://doi.org/10.1002/anie.202013594>.
- [14] S. Liang, L. Zhu, J. Hua, W. Duan, P.T. Yang, S.L. Wang, C. Wei, C. Liu, C. Feng, Fe²⁺/HClO reaction produces Fe^{IV}O²⁺; an enhanced advanced oxidation process, *Environ. Sci. Technol.* 54 (2020) 6406–6414, <https://doi.org/10.1021/acs.est.0c00218>.
- [15] Z. Zhang, Y.H. Chuang, N. Huang, W.A. Mitch, Predicting the contribution of chloramines to contaminant decay during ultraviolet/hydrogen peroxide advanced oxidation process treatment for potable reuse, *Environ. Sci. Technol.* 53 (2019) 4416–4425, <https://doi.org/10.1021/acs.est.8b06894>.
- [16] P. Zhou, W. Ren, G. Nie, X.J. Li, X.G. Duan, Y.L. Zhang, S.B. Wang, Fast and long-lasting iron(III) reduction by boron toward green and accelerated fenton chemistry, *Angew. Chem. Int. Ed.* 59 (2020) 16517–16526, <https://doi.org/10.1002/anie.202007046>.
- [17] B. Wang, Z. Cao, C. Rovira, J. Song, S. Shaik, Fenton-derived oh radicals enable the MPnS enzyme to convert 2-hydroxyethylphosphonate to methylphosphonate: insights from ab initio QM/MM MD simulations, *J. Am. Chem. Soc.* 141 (2019) 9284–9291, <https://doi.org/10.1021/jacs.9b02659>.
- [18] Q. Wang, P. Wang, P. Xu, Y. Li, J.J. Duan, G.S. Zhang, L.M. Hu, X.J. Wang, W. Zhang, Visible-light-driven photo-fenton reactions using Zn_{1-1.5}Fe_{0.5}S/g-C₃N₄ photocatalyst: degradation kinetics and mechanisms analysis, *Appl. Catal. B* 266 (2020), 1188653, <https://doi.org/10.1016/j.apcatb.2020.1188653>.
- [19] Y. Zheng, Z.H. Yu, H.H. Ou, A.M. Asiri, Y.L. Chen, X.C. Wang, Black phosphorus and polymeric carbon nitride heterostructure for photoinduced molecular oxygen activation, *Adv. Funct. Mater.* 28 (2018), 1705407, <https://doi.org/10.1002/adfm.201705407>.
- [20] L. Wu, B. Li, Y. Li, X. Fan, F. Zhang, G. Zhang, Q. Xia, W. Peng, Preferential growth of the cobalt (200) facet in Co@N-C for enhanced performance in a fenton-like reaction, *ACS Catal.* 11 (2021) 5532–5543, <https://doi.org/10.1021/acscatal.1c00701>.
- [21] B. Niu, S. E, Y. Cao, J. Xiao, L. Zhan, Z. Xu, Utilizing e-waste for construction of magnetic and core-shell z-scheme photocatalysts: an effective approach to e-waste recycling, *Environ. Sci. Technol.* 55 (2021) 1279–1289, <https://doi.org/10.1021/acs.est.0c07266>.
- [22] D. Zhao, C.L. Dong, B. Wang, C. Chen, Y.C. Huang, Z. Diao, S. Li, L. Guo, S. Shen, Synergy of dopants and defects in graphitic carbon nitride with exceptionally modulated band structures for efficient photocatalytic oxygen evolution, *Adv. Mater.* 31 (2019), 1903545, <https://doi.org/10.1002/adma.201903545>.
- [23] G. Zhang, Y. Xu, D. Yan, C. He, Y. Li, X. Ren, P. Zhang, H. Mi, Construction of k⁺ ion gradient in crystalline carbon nitride to accelerate exciton dissociation and charge separation for visible light H₂ production, *ACS Catal.* 11 (2021) 6995–7005, <https://doi.org/10.1021/acscatal.1c00739>.
- [24] P. Zhang, Y. Tong, Y. Liu, J.J.M. Vequizo, H. Sun, C. Yang, A. Yamakata, F. Fan, W. Lin, X. Wang, W. Choi, Heteroatom dopants promote two-electron O₂ reduction for photocatalytic production of H₂O₂ on polymeric carbon nitride, *Angew. Chem. Int. Ed.* 59 (2020) 16209–16217, <https://doi.org/10.1002/anie.202006747>.
- [25] Y. Xie, Y.X. Li, Z.H. Huang, J.Y. Zhang, X.F. Jia, X.S. Wang, J.H. Ye, Two types of cooperative nitrogen vacancies in polymeric carbon nitride for efficient solar-driven H₂O₂ evolution, *Appl. Catal., B* 265 (2020), 118581, <https://doi.org/10.1016/j.apcatb.2019.118581>.
- [26] S. Wu, H.T. Yu, S. Chen, X. Quan, Enhanced photocatalytic H₂O₂ production over carbon nitride by doping and defect engineering, *ACS Catal.* 10 (2020) 14380–14389, <https://doi.org/10.1021/acscatal.0c03359>.
- [27] X. Li, X. Yang, Y. Huang, T. Zhang, B. Liu, Supported noble-metal single atoms for heterogeneous catalysis, *Adv. Mater.* 31 (2019), 1902031, <https://doi.org/10.1002/adma.201902031>.
- [28] P. Zhang, Y. Rao, Y. Huang, M. Chen, T. Huang, W. Ho, S. Lee, J. Zhong, J. Cao, Transformation of amorphous Bi₂O₃ to crystal Bi₂O₂CO₃ on Bi nanospheres surface for photocatalytic NO_x oxidation: intensified hot-electron transfer and reactive oxygen species generation, *Chem. Eng. J.* 420 (2021), 129814, <https://doi.org/10.1016/j.cej.2021.129814>.
- [29] G. Prusty, J.T. Lee, S. Seifert, B.B. Muhoberac, R. Sardar, Ultrathin plasmonic tungsten oxide quantum wells with controllable free carrier densities, *J. Am. Chem. Soc.* 142 (2020) 5938–5942, <https://doi.org/10.1021/jacs.9b13909>.
- [30] T. He, C. Jiang, J. He, Y. Zhang, G. He, J. Wu, J. Lin, X. Zhou, P. Huang, Manganese-dioxide-coating-instructed plasmonic modulation of gold nanorods for activatable duplex-imaging-guided nir-ii photothermal-chemodynamic therapy, *Adv. Mater.* 33 (2021), 2008540, <https://doi.org/10.1002/adma.202008540>.
- [31] H.W. Zhang, T. Itoi, T. Konishi, Y. Izumi, Dual photocatalytic roles of light: Charge separation at the band gap and heat via localized surface plasmon resonance to convert CO₂ into CO over silver-zirconium oxide, *J. Am. Chem. Soc.* 141 (2019) 6292–6301, <https://doi.org/10.1021/jacs.8b13894>.
- [32] A. Kuila, P. Saravanan, D. Bahnemann, C. Wang, Novel Ag decorated, biocatal surface doped AgVO₃ nanobelt ternary composite with z-scheme homojunction-heterojunction interface for high prolific photo switching, quantum efficiency and hole mediated photocatalysis, *Appl. Catal. B* 293 (2021), 120224, <https://doi.org/10.1016/j.apcatb.2021.120224>.
- [33] C. Feng, L. Tang, Y. Deng, J. Wang, J. Luo, Y. Liu, X. Ouyang, H. Yang, J. Yu, J. Wang, Synthesis of leaf-vein-like g-C₃N₄ with tunable band structures and charge transfer properties for selective photocatalytic H₂O₂ evolution, *Adv. Funct. Mater.* 30 (2020), 20001922, <https://doi.org/10.1002/adfm.202001922>.
- [34] Z. Qiu, C.-W. Tai, G.A. Niklasson, T. Edvinsson, Direct observation of active catalyst surface phases and the effect of dynamic self-optimization in NiFe-layered double hydroxides for alkaline water splitting, *Energy Environ. Sci.* 12 (2019) 572–581, <https://doi.org/10.1039/C8EE03282C>.
- [35] C.C. Wu, H.Q. Li, Z.X. Xia, X.M. Zhang, R.Y. Deng, S.L. Wang, G.Q. Sun, NiFe layered double hydroxides with unsaturated metal sites via precured surface strategy for oxygen evolution reaction, *ACS Catal.* 10 (2020) 11127–11135, <https://doi.org/10.1021/acscatal.0c02501>.
- [36] Z.W. Chen, M. Ju, M.Z. Sun, L. Jin, R.M. Cai, Z. Wang, L. Dong, L.M. Peng, X. Long, B.L. Huang, S.H. Yang, T.M. LDH meets birnessite: a 2d-2d hybrid catalyst with long-term stability for water oxidation at industrial operating conditions, *Angew. Chem. Int. Ed.* 60 (2021) 9699–9705, <https://doi.org/10.1002/anie.202016064>.
- [37] H.R. Sun, F. Guo, J.J. Pan, W. Huang, K. Wang, W.L. Shi, One-pot thermal polymerization route to prepare n-deficient modified g-C₃N₄ for the degradation of tetracycline by the synergistic effect of photocatalysis and persulfate-based advanced oxidation process, *Chem. Eng. J.* 406 (2021), 126844, <https://doi.org/10.1016/j.cej.2020.126844>.
- [38] R. Bhosale, S. Jain, C.P. Vinod, S. Kumar, S. Ogale, Direct z-scheme g-C₃N₄/FeWO₄ nanocomposite for enhanced and selective photocatalytic CO₂ reduction under

- visible light, *ACS Appl. Mater. Interfaces* 11 (2019) 6174–6183, <https://doi.org/10.1021/acsami.8b22434>.
- [39] Y. Lin, H. Wang, C.K. Peng, L. Bu, C.L. Chiang, K. Tian, Y. Zhao, J. Zhao, Y.G. Lin, J. M. Lee, L. Gao, Co-induced electronic optimization of hierarchical nife ldh for oxygen evolution, *Small* 16 (2020), 2002426, <https://doi.org/10.1002/sml.202002426>.
- [40] S. Lee, L. Bai, X. Hu, Deciphering iron-dependent activity in oxygen evolution catalyzed by nickel-iron layered double hydroxide, *Angew. Chem. Int. Ed.* 59 (2020) 8072–8077, <https://doi.org/10.1002/anie.201915803>.
- [41] J.G. Li, H. Sun, L. Lv, Z. Li, X. Ao, C. Xu, Y. Li, C. Wang, Metal-organic framework-derived hierarchical (Co,Ni)Se₂@NiFe LDH hollow nanocages for enhanced oxygen evolution, *ACS Appl. Mater. Interfaces* 11 (2019) 8106–8114, <https://doi.org/10.1021/acsami.8b22133>.
- [42] H. Xu, C. Shan, X. Wu, M. Sun, B. Huang, Y. Tang, C.-H. Yan, Fabrication of layered double hydroxide microcapsules mediated by cerium doping in metal-organic frameworks for boosting water splitting, *Energy Environ. Sci.* 13 (2020) 2949–2956, <https://doi.org/10.1039/D0EE02113J>.
- [43] J. Ma, S.W. Gao, Plasmon-induced electron-hole separation at the Ag/TiO₂(110) interface, *ACS Nano* 13 (2019) 13658–13667, <https://doi.org/10.1021/acsnano.9b03555>.
- [44] P.F. Xia, M. Antonietti, B.C. Zhu, T. Heil, J.G. Yu, S.W. Cao, Designing defective crystalline carbon nitride to enable selective CO₂ photoreduction in the gas phase, *Adv. Funct. Mater.* 29 (2019), 1900093, <https://doi.org/10.1002/adfm.201900093>.
- [45] D. Zhou, S. Wang, Y. Jia, X. Xiong, H. Yang, S. Liu, J. Tang, J. Zhang, D. Liu, L. Zheng, Y. Kuang, X. Sun, B. Liu, NiFe hydroxide lattice tensile strain: enhancement of adsorption of oxygenated intermediates for efficient water oxidation catalysis, *Angew. Chem. Int. Ed.* 58 (2019) 736–740, <https://doi.org/10.1002/anie.201809689>.
- [46] M. Shakeel, M. Arif, G. Yasin, B.S. Li, H.D. Khan, Layered by layered Ni-Mn-LDH/g-C₃N₄ nanohybrid for multi-purpose photo/electrocatalysis: morphology controlled strategy for effective charge carriers separation, *Appl. Catal. B* 242 (2019) 485–498, <https://doi.org/10.1016/j.apcatb.2018.10.005>.
- [47] D. Han, D.Y. Ni, Q. Zhou, J.J. Ji, Y.Q. Lv, Y.F. Shen, S.Q. Liu, Y.J. Zhang, Harnessing photoluminescent properties of carbon nitride nanosheets in a hierarchical matrix, *Adv. Funct. Mater.* 29 (2019), 1905576, <https://doi.org/10.1002/adfm.201905576>.
- [48] S.J. Jian, Z.W. Tian, J.P. Hu, K.Y. Zhang, L. Zhang, G.G. Duan, W.S. Yang, S. H. Jiang, Enhanced visible light photocatalytic efficiency of La-doped ZnO nanofibers via electrospinning-calcination technology, *Adv. Powder Mater.* (2021), <https://doi.org/10.1016/j.apmate.2021.09.004>.
- [49] H.Y. Jing, P. Zhu, X.B. Zheng, Z.D. Zhang, D.S. Wang, Y.D. Li, Theory-oriented screening and discovery of advanced energy transformation materials in electrocatalysis, *Adv. Powder Mater.* (2021), <https://doi.org/10.1016/j.apmate.2021.10.004>.